Heritage Science

RESEARCH

Open Access

Pulsed infrared thermographic study of a Chinese Bronze Lei

Xue Yang[1], Beichen Chen[2*], Gangbo Hu[1], Xiangyu Wang[1], Wei Fang[1], Jianan Zhang[2], Ning Tao[1] and Guangkuo Yuan[2]

Abstract

In this paper, pulsed infrared thermography is applied to the study of a mold casting Chinese bronze *lei* 罍 dated to the late Shang dynasty (c.a.1250–1050 BC), currently housed in the Capital Normal University Museum. Many spacers and a defective area of this ancient bronze are partly covered with repair material. By analyzing thermographic images using a one-layer thermal diffusion model, it is found that the spacers were specifically made for this bronze. The thickness of the repairing material in the defective area is measured using thermal quadrupole modelling in multi-layer materials. This is the first application of this method to the field of cultural heritage conservation. These results provide a deeper understanding of the manufacturing process of ancient Chinese bronzes from the viewpoint of archaeological research. They also help assess the repair status from the conservation viewpoint.

Keywords: Chinese bronze vessels, Pulsed infrared thermography, Mold casting spacers, Restoration trace, Thermal quadrupole method

Introduction

In ancient China, the main technique used to produce bronze ritual vessels was mold casting, a method also known as piece-mold casting 块范法. A clay mold was created, often using a model of the object to be made. The mold pieces were then fired and reassembled around a clay core, leaving a narrow cavity that was filled with a molten bronze alloy. A hollow vessel would result after the removal of the entire mold system [1]. To preserve the integrity of the cavity, craftsmen sometimes put spacers into it, a technique similar to the chaplets used in lost-wax casting to fix the distance between the core and the mold. The usage of spacers has been studied since the mid-twentieth century. The Japanese scholar Matsumaru Michio and others carried out systematic studies on spacer by locating them from direct observation and ink rubbings of the bronzes [2]. The study of these artifacts is now much easier thanks to the development of imaging methods such as X-ray and industrial computed tomography (CT).

Many scholars have carried out X-ray and CT analysis of ancient Chinese bronzes to examine defects and repairs, as well as to investigate the casting process [3, 4]. However, both methods have problems. X-ray imaging is constrained by the transmission imaging principle. In vessels such as *hu* 壶, *ding* 鼎, *gui* 簋, the front and back walls will be overlaid together in the images, making it difficult to distinguish the characteristic properties, as mentioned in Ref. [4]. CT technology, on the other hand, solves the overlay problem, but is affected by safety, mobility and applicability issues. Other imaging techniques such as multi-spectral imaging (MSI), hyperspectral imaging (HSI) and reflectance transformation imaging (RTI) etc. lack the ability to assess subsurface conditions.

Infrared thermography (IRT) is a non-contact, nondestructive testing (NDT) technique to detect surface and subsurface structural or material inhomogeneities based on the evaluation of surface temperature changes of an

*Correspondence: chen_beichen@cnu.edu.cn

[2] School of History, Capital Normal University, 83 West Third Ring Road North, Beijing 100089, China
Full list of author information is available at the end of the article

object. It can be carried out actively or passively depending on whether a thermal excitation is applied on the object or not. Photo-thermal excitation is the most common excitation method for IRT. It can be conducted using flash lamps, halogen lamps and lasers. Active thermography can be further sub-divided into pulsed thermography (PT), lock-in thermography (LIT), step-heating thermography (ST) and so on. Moreover, active IRT can be carried out in both reflection and transmission geometry depending on whether excitation and observation take place on the same or opposite sides of the object. There are two main applications for IRT: (1) qualitative applications, where defects and flaws are identified using image processing methods; (2) quantitative applications, where thermal parameters and features such as defect depth are determined using heat transfer theory [5, 6].

During the last two decades, IRT has been extensively applied to investigate different types of cultural heritages and artifacts with various thermal properties [7–9], such as historical buildings [10, 11], paintings on canvas or wood [12], murals or frescos [13, 14], plastered mosaics [15, 16], as well as metal artifacts [17–23]. The study of metal objects is typically conducted using pulsed IRT due to its relatively high thermal conductivity and diffusivity. In previous works, IRT is mostly applied to Western bronze statues casted by lost-wax method. A heat diffusion model for a single layer sample with finite thickness [17–22] is employed for pulsed thermography in reflection geometry. Furthermore, a double-layer structure is considered in Ref. [23], where thermal heat conductance is used to characterize the interface heat transfer efficiency. While mold casting bronzes are usually made in the shape of vessels, if necessary, IRT can be performed in both reflection and transmission geometry. Moreover, the bronze wall thickness is relatively thin and bare with complicated bronze corrosion products on both sides due to a long underground history. Therefore, a high acquisition frequency is required for a fast thermal transfer process and a thermal diffusion theory for a multi-layer structure is usually applied for analyzing the thermal behavior.

The purpose of this work is to examine a bronze vessel lei's situation behind the historical restoration trace in order to analyze the original casting procedure and the current preservation status in the context of both archaeology and conservation. An unusually large number of spacers are found in the vessel, including some partially or fully covered by repairing materials. Additionally there is a large area with repairing marks. We conduct pulsed thermography measurements to determine the spacers' material, shape and merging conditions with the vessel body. We also investigate the shape of the defects and the thickness of the repairing material on the large repairing area. An analytical model was applied to characterize the spacers quantitatively, assuming a single-layer structure, and qualitatively, assuming a double-layer structure. The thermal quadrupole method was utilized to analyze quantitatively the layered structures in the large repairing area.

Material and methods

Research object

The bronze ritual vessel *lei*, a wine container with many spacers, is inspected. The sample is 46 cm in height and barely decorated. It has two shoulder handles with hanging rings that flanked the body, and a belly handle on its back side, which helps to tilt the body when the vessel is in use, as shown in Fig. 1b. All three handles are in the shape of buffalo heads. The shoulder band is decorated with six whorl circles, which are evenly distributed between the two shoulder handles. The vessel can be typologically dated to the late Shang dynasty (c.a. 1250–1050 BC).

A visual inspection reveals more than 50 spacers on the vessel body. They belong to eight registers: two registers on the neck (6 spacers each); one on the shoulder (9 spacers); four on the belly (12, 9, 7, and 5 spacers); and one on the foot (8 spacers). The belly spacers are generally larger than those on the neck and foot. They can be classified into two groups in terms of their current conditions: (1) unrepaired spacers; and (2) repaired spacers. Furthermore, there is a large, repaired defective area on the front side of the vessel body. The diameter of this area is approximately 5 cm, as shown in Fig. 1a indicated by an arrow.

Pulsed thermography methods

In pulsed thermography, the front surface of the sample is heated by a short pulse of light. The heat generated at the front surface propagates to the interior of the sample. An infrared camera captures the time dependent temperature change on the surface of the object. The 1D time-dependent surface temperature increase T $(z = 0)$ for a homogeneous sample with semi-infinite thickness $(l = \infty)$ is described by [24]:

$$T(0,t)_{l=\infty} = \frac{Q}{e\sqrt{\pi t}}, \tag{1}$$

where Q is the absorbed energy density on the surface, and e is the effusivity of the sample ($e = \sqrt{k\rho C}$, with k, ρ and C the thermal conductivity, density, and the specific heat of the sample, respectively).

Fig. 1 Photographs of the Chinese bronze *lei*

For a slab sample of finite thickness l, the temperature change at the front surfaces is:

$$T(0,t) = \frac{Q}{\rho C l}\left[1 + 2\sum_{n=1}^{\infty} exp(\frac{-n^2\pi^2\alpha t}{l^2})\right], \quad (2)$$

for measurements performed in reflection [25]. The surface temperature evolves as $t^{-0.5}$ at early times, as expected from Eq. (1), and then approaches a stationary value when the heat reaches the sample's opposite side. At thermal equilibrium ($t = \infty$), the surface temperature can be yield readily from Eq. (2) [26]:

$$T(0,\infty) = \frac{Q}{\rho C l} \quad (3)$$

The sample thickness and thermal diffusivity ($\alpha = k/(\rho C)$) are related by a characteristic time [27]

$$t_c = \frac{l^2}{\pi\alpha}, \quad (4)$$

which corresponds to the intersection point of the curves derived from Eqs. (1) and (3). We define the normalized temperature $V = T(0,t)/T(0,\infty)$ and plot $\ln V$ as a function of the logarithm of the normalized time $\omega = \pi^2\alpha t/l^2$ (Fig. 2). The $\ln V$ (solid line) follows the trend described by Eq. (2) and then Eq. (4). The first derivative of $\ln V$ (dashed-dot line) is -0.5 at first and approaches zero for larger times. The second derivative (dashed line) is zero at early and later time periods, and reaches a maximum in between. Shepard et al. proposed to use the peak in the second derivative of the surface temperature to determine t_c [27].

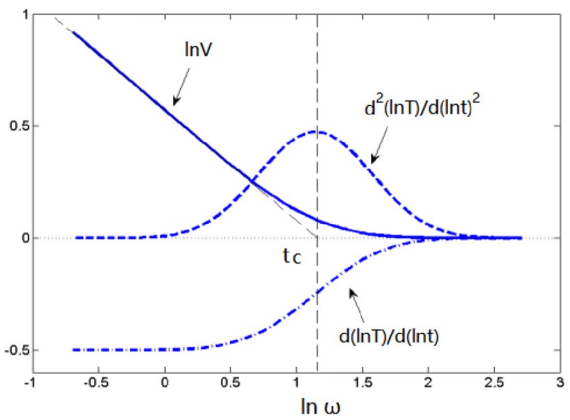

Fig. 2 Normalized logarithmic surface temperature and its first and second logarithmic derivatives as a function of the nondimensional time for a single-layer structure with finite thickness under pulsed thermal excitation

When the sample consists of two layers and the second layer can be considered as semi-infinite, the surface temperature decay is [28]:

$$T(0,t) = \frac{Q}{e_1\sqrt{\pi t}}\left[1 + 2\sum_{n=1}^{\infty}\left(\frac{e_1 - e_2}{e_1 + e_2}\right)^n exp\left(-n^2\frac{l_1^2}{\alpha_1 t}\right)\right], \quad (5)$$

where e_1 and e_2 are the effusivities of the first and the second layer. The first derivative of T logarithm with respect to time logarithm is plotted in Fig. 3. A peak is observed because the thermal wave encounters an interface of materials with different thermal properties. The peak

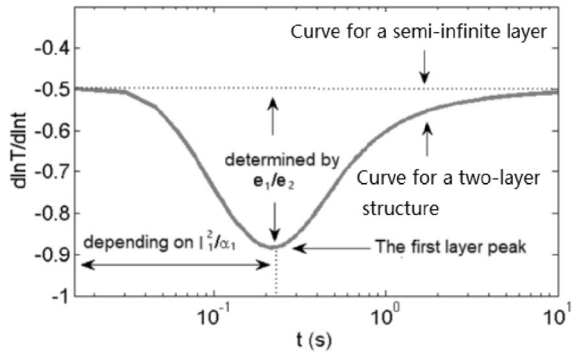

Fig. 3 First logarithmic derivative of surface temperature for a double-layer structure with semi-infinite second layer under pulsed thermal excitation

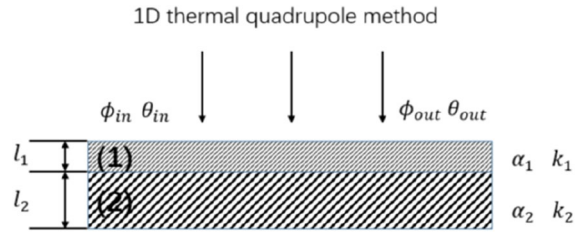

Fig. 4 Schematic of heat transfer modeling for a double-layer structure

position is related to the thickness and thermal diffusivity of the first layer, and its amplitude is determined by the ratio of the effusivities of the two layers. By analyzing this curve, we can characterize the material characteristics of different layers [29]. When the second layer cannot be considered as semi-infinite, the peak amplitude and position will both depends on the properties of the second layer the logarithmic derivative will be larger than − 0.5, the value that describes a semi-infinite structure. In this case, the analytical solution becomes complicated and requires tedious calculations, especially in finding the roots of complex transcendent equations [26].

A simpler solution is to solve the multilayer heat conduction problem using the thermal quadrupole method [30], which allows us to derive algebraic solutions in the Laplace domain. The dependence of the 'Laplace temperature' on different layer parameters can be analyzed in Laplace space, and the return to real temperatures is done by applying numerical algorithms. For 1D multilayered materials, the numerical inverse Laplace transform of an analytical solution is possible for many configurations and is often much faster and more accurate than finite difference or finite element techniques for the same configuration. It has also been shown to be applicable for 2D and 3D configurations [31]. In the thermal quadrupole method, the response of a multilayer system is calculated using matrix multiplication, as shown in Eq. 6, where ϕ_{in}, θ_{in}, ϕ_{out} and θ_{out} are the input and output Laplace temperatures and flux (i.e. the four poles) and M_i is the transition matrices relative to layer i.

The Laplace variable is p and l_i, α_i and k_i are the thickness, thermal diffusivity and thermal conductivity of the layer i, respectively. Here we ignore the convective heat loss and thermal resistance between layers. A double-layer model is presented in Fig. 4.

Experimental design

A schematic diagram of the pulsed IR thermography experiment for the investigation of the bronze *lei* is shown in Fig. 5. A reflection experimental geometry is adopted. Two flash lamps with 4.8 kJ energy in total are used to excite the sample. The flash duration is 2 ms. The thermal emission is detected using a cooled long wave infrared camera with a HgCdTe (MCT) detector with spectral response from 7.7 to 9.3 μm and 320 × 256 pixels. The noise equivalent temperature difference (NETD) is less than 20 mK at 25 °C. The full frame rate is 225 Hz, and higher sampling frame rates are possible with sub-windowing modes. The bronze vessel's wall thickness was measured by a special caliper gauge with the accuracy of ± 0.15 mm.

Two experimental campaigns are carried out with different experimental parameters. In the first campaign, measurements are taken of all the visible and suspected spacers. The frame rate used is 2000 Hz with a window size of 80 × 64 pixels and 2 s capturing time. For this parameter settings, the flash excitation will be captured by several frames. t = 0 frame is defined as the frame that the IR camera has the highest averaged digital level. In the second campaign, measurements of the repaired area are taken. The frame rate is 225 Hz with full window size and 5 s capturing time.

$$\begin{bmatrix} \theta_{in} \\ \phi_{in} \end{bmatrix} = \prod_{i}^{n-layers} M_i \begin{bmatrix} \theta_{out} \\ \phi_{out} \end{bmatrix} \text{with} M_i = \begin{bmatrix} \cosh\left(\sqrt{\frac{p}{\alpha_i}} l_i\right) & \frac{\sinh\left(\sqrt{\frac{p}{\alpha_i}} l_i\right)}{\sqrt{\frac{p}{\alpha_i}} k_i} \\ \sqrt{\frac{p}{\alpha_i}} k_i \sinh\left(\sqrt{\frac{p}{\alpha_i}} l_i\right) & \cosh\left(\sqrt{\frac{p}{\alpha_i}} l_i\right) \end{bmatrix} \quad (6)$$

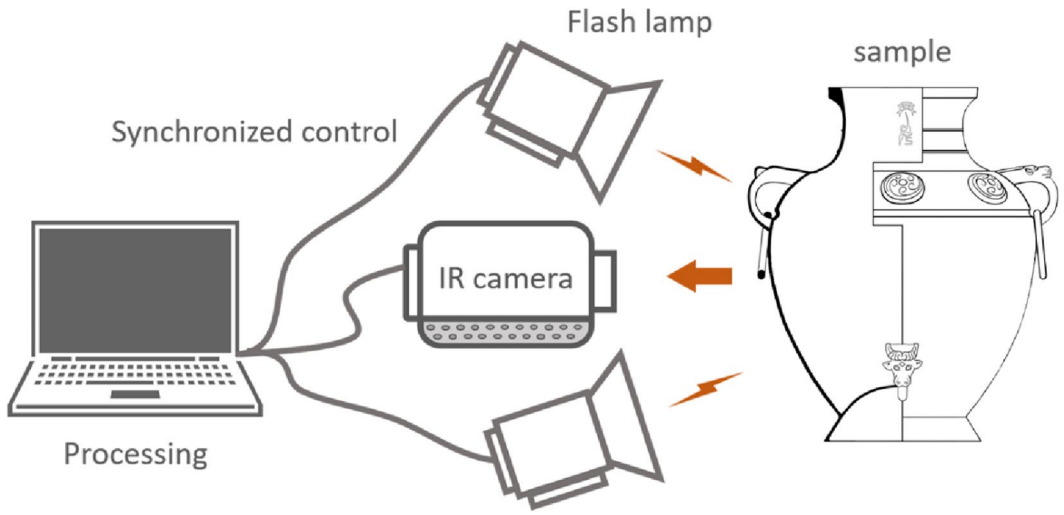

Fig. 5 Experimental setup for the inspection of the sample *lei*

Results and discussion

Spacers

The two types of spacers, with repairs and without repairs, are shown in Fig. 6. The spacers on the top two registers have no repairing marks. The edges are clear with rust around the spacer, as shown in Fig. 6a. Spacers with repairs are mostly found on the third to the sixth registers. In some cases, the repair material only covers the edges of a spacer, but sometimes it covers the whole area, as shown in Fig. 6b. With so many spacers in use, one will wonder whether those spacers were specifically made for this vessel or whether they were recycled from failed products. Other matters for investigation are how the alloy composition compares with the main body, and the condition of the casting under the repairs. Therefore careful examination is carried out to investigate the following aspects in a non-contact fashion: the shape of the spacers, their materials, and the relationships between them and the main body.

Shape

The IRT method is firstly used to examine the situations below the repairing layer. A typical spacer with edges covered by repairs is shown in Fig. 7 as an example. Figure 7a is the photograph of the spacer and (b-d) are its thermal images at different times after flash excitation. The longer the delay, the deeper into the object we can observe. When the flash pulse arrives, the temperature of

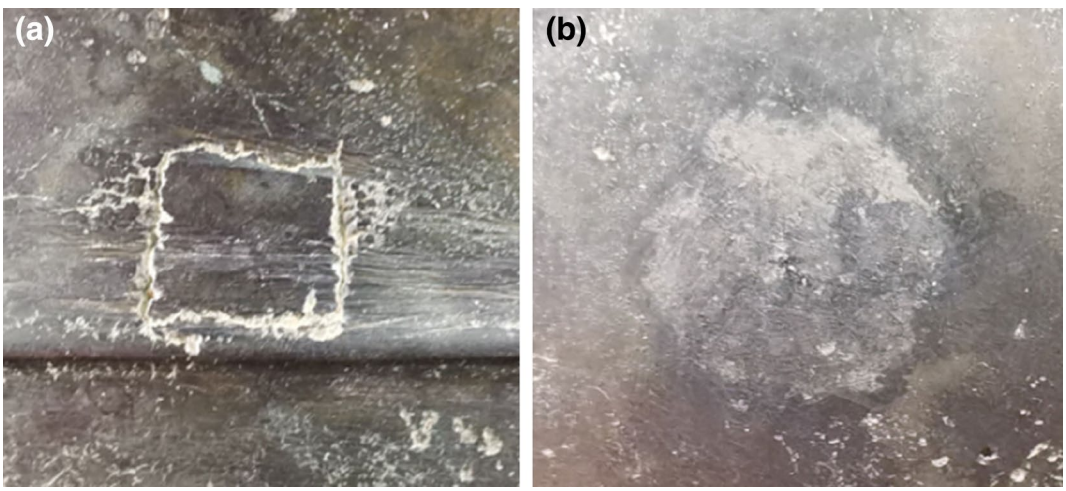

Fig. 6 Photograph of two types of spacers **a** without repair and **b** with repair

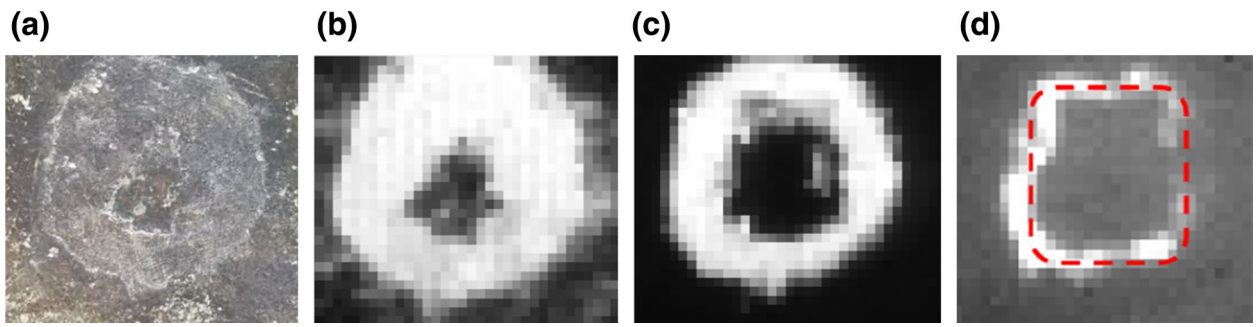

Fig. 7 Photograph (**a**) and thermal images (**b**–**d**) of the spacer with repairs on the edge (the flash frame (**b**), 25 ms (**c**), and 500 ms (**d**) after flash excitation). Each of the thermal images are optimized in contrast

the repairing material is higher due to higher absorptivity and emissivity. After 25 ms, as shown in Fig. 7c, the thermal energy has diffused into the subsurface, causing the central area to become enlarged. Figure 7d reveals the spacer's original shape under the surface repair, as indicated by the dashed square. Meanwhile, it can be observed that the gap on the left side of the spacer is more pronounced than on the right side.

Figure 8 shows the photograph and thermal images of an area fully covered by repairs. After examining the sequential thermal images, we find that under the surface repair, the irregular shape soon becomes a square shape, as shown in Fig. 8c and d. At later time the square shape becomes not so obvious in Fig. 8d is due to the repairing material layer is uneven. Most of the spacers are in rectangular or square shape, judged by direct observation and by IR thermography, indicating that they are specifically prepared for the use as spacers.

Material

If the spacers were specifically made for this object, were they made using an alloy with the same composition as the body or not? We selected a belly spacer with clear edges and a clean surface to investigate its thermal parameters. The central area on the spacer and an adjacent area on the main body are selected, as shown in Fig. 9a. Their cooling curves after flash lamp excitation are plotted in Fig. 9b. The thermal response of the two areas is very similar, with only the first few frames not overlapping with each other. The second derivative of the surface temperature in logarithmic scale further supports this argument. As shown in Fig. 9c, the earlier peak is due to the flash duration effect, which normally lasts a few milliseconds, and the second peak (marked by black stars in Fig. 9c) can be used to determine the characteristic time t_c [32], as illustrated in Fig. 1. From the measured thickness of 2.1 mm at these positions and the characteristic times t_c of 114 ms and 108 ms, we obtain the material thermal diffusivities of 12 mm^2/s and 13 mm^2/s for the spacer and the main body. Similar values have been obtained for measurements taken on other spacers and areas of the vessel. As a consequence, it is likely that the spacer and the main body are made of the same type of alloy. Errors could be due to the inaccuracy of the thickness measurement and thin rust layers on the front and back surface.

To further investigate the repairing materials, we choose four areas on the *lei*'s belly, marked with colored

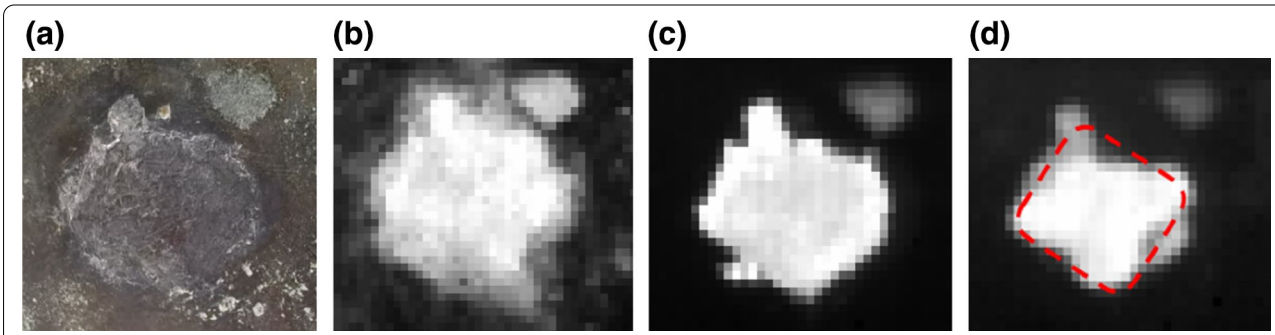

Fig. 8 Photograph (**a**) and thermal images (**b**–**d**) of the repair covered area (the flash frame (**b**), 25 ms (**c**), and 500 ms (**d**) after flash excitation). Each of the thermal images are optimized in contrast

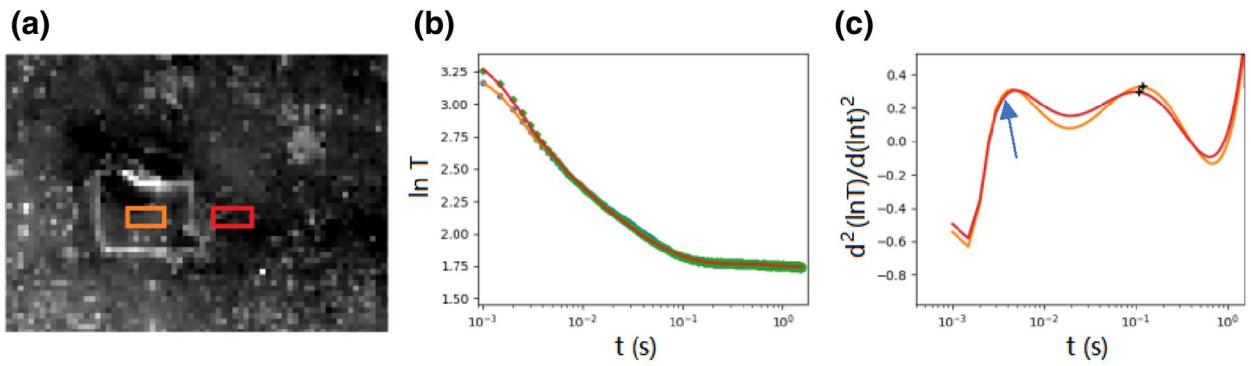

Fig. 9 Single-layer structure analysis: **a** the thermal image of a spacer and the adjacent area; **b** the original data in log–log scale with 7th order polynomial fitting and **c** the second derivative of the fitting curve in log scale with the pointed flash peak and marked 1st layer characteristic peak

squares in Fig. 10a. They are numbered from 1 to 4 on the thermal image in Fig. 10b. No. 1 and 2 are spacers fully covered by repairing materials and No. 3 and 4 are with repairs only on the edge. Figure 10c shows the first derivative of the logarithmic surface temperature. Curves 1 and 2 show the typical behavior of a two layer structure, while curves 3 and 4 demonstrate a single layer behavior. The presence of a two-layer structure excludes the possibility that the hole was a through hole before repair. Therefore, it is unlikely the spacer would have loosened and gone missing. The negative peaks pointing downwards indicate that the repairing material has a smaller effusivity than the bronze substrate. The amplitude of the curves 1 and 2 indicates a large effusivity difference between the two materials. Therefore, we can conclude that the repairing material is likely to be color matched plaster rather than metallic material. It is not possible to identify the first layer thickness or thermal parameter from the peak's position accurately from Fig. 10c, since the substrate thickness has a significant effect when it is relatively thin.

Merging

During casting, the spacers are surrounded by molten metal poured inside the cavity from the sprues of the mold system. The merging conditions of different spacers could be different, depending on how quickly the molten metal meets the spacer. Even the edges of the same spacer could show differences in different directions. By carefully studying the IRT data of each spacer on the belly, we find that 23 out of 30 spacers have their lower edge merged better with the main body of the vessel under the repairing material, as shown in Fig. 11a, b. For vessel shaped bronzes, it has been generally agreed that the sprues were designed at the bottom of the vessel in the mold system. The orientation of the better merged

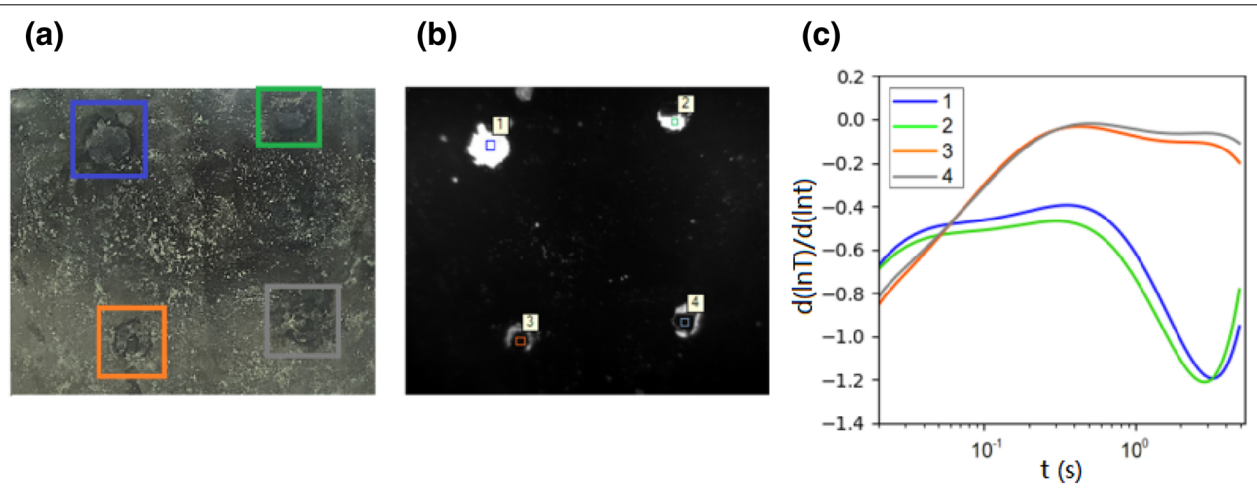

Fig. 10 Single and double-layer structure analysis. **a** Photograph, **b** thermal image of four spacers and **c** first derivative of a 7^{th} order polynomial fitting of the surface temperature

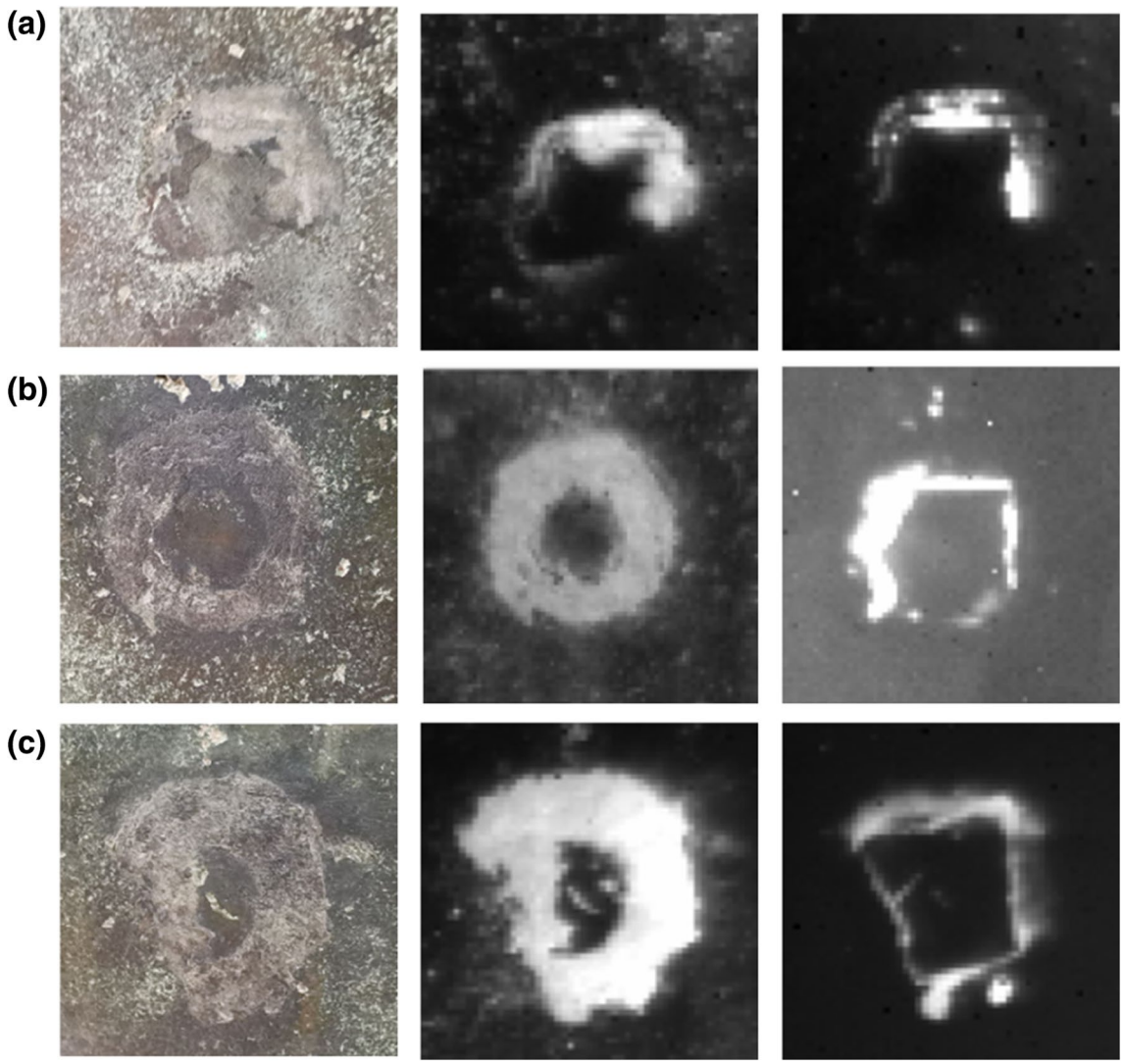

Fig. 11 Merging conditions

edges might also support this conclusion. Moreover, we find there are small voids filled with repairing material originating from air bubbles formed in the casting procedure, as illustrated in Fig. 11c.

Repairs on the defective area

In the previous section, we mainly focused on the shape, material and merging conditions of the spacers within the main body. On this *lei* vessel, there is also a large (5.0 cm in diameter) repairing mark on the belly. We therefore took IRT measurements of this area. Photographs, as shown in Fig. 12a, reveal that this area is covered with repairing material, which prevents us from inspecting the condition of the subsurface. A thermal image immediately after flash excitation is shown Fig. 12b, where the boundary of the repairing area are clearly visible. Figure 12c, d are the thermal images taken 0.64 s and 2 s after flash excitation, respectively. It is revealed that under the surface there is an oval-shaped metal material with two crescent-shaped areas on each side of it, which are filled with more repairing material deeper inside the body.

The region marked with a red square in Fig. 12c has been examined in more details. Three areas are selected, as shown in Fig. 13a. The IR signal decay (symbols) and the corresponding polynomial fittings (lines) are shown in Fig. 13b. The first derivative of the fitting curves (orange) and experimental data (blue) in log–log scale are plotted in Fig. 14a, c, e. It can be seen that the fitting curves are in good agreement with the original raw data and precisely

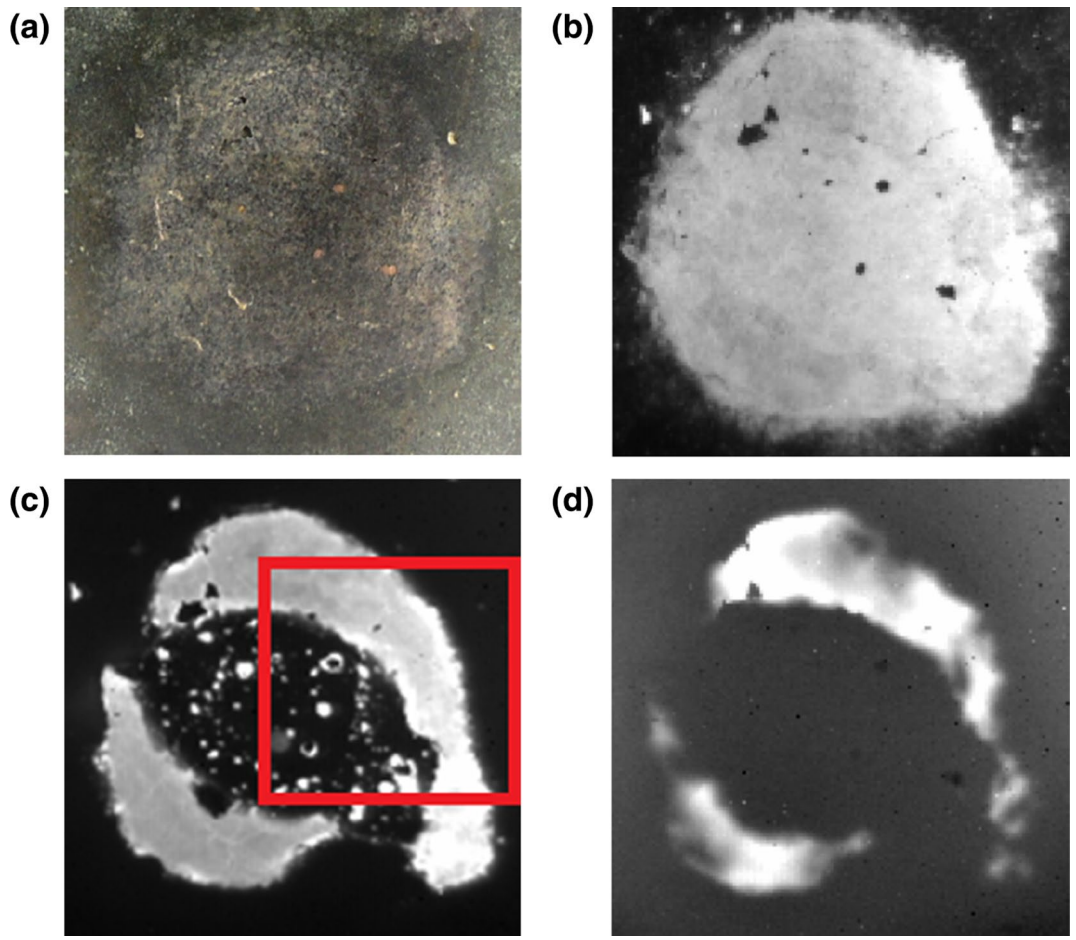

Fig. 12 Photograph of the defective area (**a**) and corresponding thermal images of the flash frame, and 0.64 s and 2 s after flash excitation (**b**–**d**)

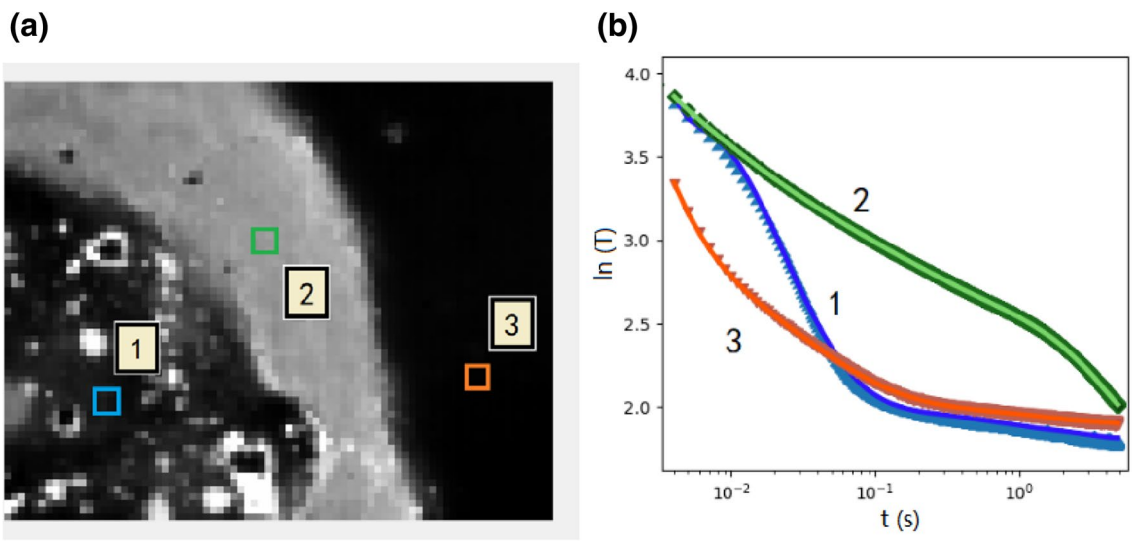

Fig. 13 **a** Thermal image of the top right corner of the repaired area, **b** the surface temperature decay in log–log scale (symbols) and the polynomial fitting (lines)

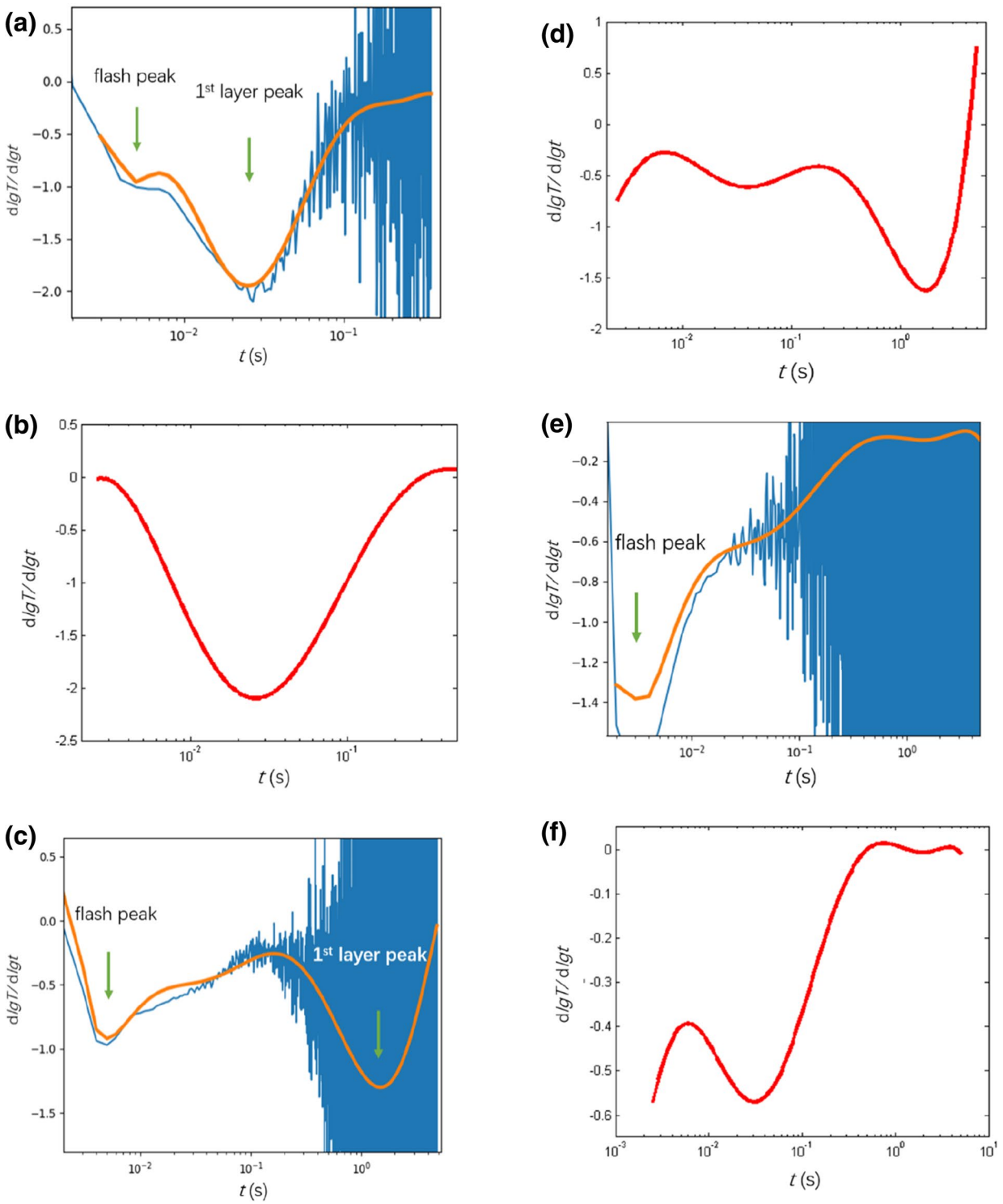

Fig. 14 The first derivative of the fitting curve (orange) and experimental data (blue) as a function of time in log–log scale (**a**, **c**, **e**) and the thermal response calculated from a double-layer thermal quadrupole model (**b**, **d**, **f**) for the three marked positions with $l_1 = 0.1$, 0.8 and 2.5 mm, respectively

reproduce the flash and layer peaks' position. All curves show a clear flash peak, as indicated in the figures. The curves at position 1 and 2 display strong 1st-layer peaks, as described in Fig. 3. The flash peak is superimposed over the 1st-layer peak at position 1. At position 2, the double-layer structure is assured by visual observation from the inner side of the lei vessel. The curve at position 3 shows a single layer behavior, which is in line with our expectations.

To obtain quantitative information, thermal quadrupole simulations were performed for the three positions using a double-layer model. The thermal parameters required for the simulations are listed in Table 1. The thermal parameters of the bronze substrate is measured with the flash method in reflection geometry. The IR signal decay curve is fitted using Eq. 2 for a single-layer, finite-thickness plate. The result is in agreement with the value obtained using the different methods described in Sect. 4.1.2. The repairing material's parameter is taken from pure plaster [33]. The *lei's* wall thickness at position 1, 2 and 3 are measured as 2.5 mm, i.e. $l_1 + l_2 = 2.5$mm, where l_1 and l_2 refer to the thickness of the plaster and the bronze substrate, respectively. When l_1 is 0.1 mm and 0.8 mm we have the 1st layer peak of the simulation curve at the same position of the experimental data at position 1 and 2, respectively. For position 3, $l_2 = 0$ and the simulation result is in good agreement with the experimental data.

The observation of the subsurface condition in this area leads us to recover the conservation condition. This large area defect is probably formed during or after excavation, but it could also be caused by casting flaws. Walls with inhomogeneous thickness can form in the casting process if the molten bronze cools before it completely fills the mold cavity, or if the mode cavity is thinner in some areas. In some extreme cases, misruns will occur leaving through holes on the vessel wall. This type of defect is often found away from the sprues and accompanied with porosity due to the shrinkage in the solidification process when there is insufficient liquid metal. From Fig. 12c we can see that the metal in the central area is porous, which could be due to misrun in the casting process or degradation of the material due to rusting. However, in both cases, the strength is significantly reduced in this area. Therefore, the previous conservator did not only fill the surrounding area but also covered the central metal part with repairing material. If the cause of this defect is related to the original casting flaw, rather than purely from damage before or after excavation, it might be connected to the large number of spacers inserted, which slows down the speed of molten metal filling up the cavity. Further investigation is required by examining more objects.

Table 1 List of sample thermal properties

	Thermal diffusivity	Thermal conductivity
Plaster	0.375 mm^2/s	0.301 W/(m K)
Bronze	12 mm^2/s	43 W/(m K)

Conclusion

In this paper, pulsed IRT is successfully employed in the study of a mode casting bronze *lei* from ancient China. This object contains many spacers together with a large repairing area, attracting researcher's attention in both the fields of archaeology and conservation. First, the spacers are investigated. Thermal images reveal that most of them have regular shapes and similar thermal properties as the main body. Therefore, we conclude that these spacers were likely made specifically for this vessel, rather than recycled. By examining the thermal images of all the spacers, a better merging direction around each spacer can be determined, which helps us to confirm the sprues position on the foot. Secondly, IRT is also applied to study a large repaired area. Thermal images show that under the surface there is a porous metal part surrounded by two crescent-shaped areas with thicker repairing material. With the help of the thermal quadrupole model, the thickness of the repairing layer is determined. Results reveal that this area is significantly weaker than expected and requires careful checks on a regular basis. This defect could be caused by damage during or before excavation. It could also be related to a casting flaw or misrun, since too many inserted spacers slow down the speed of molten metal filling the cavity.

Preliminary results shown in this paper demonstrate that the IRT technique is a competitive NDT method to investigate vessel shaped bronzes. Analytical solutions can be used to characterize the object's material and size. However, artifacts, especially from ancient times, usually present more complicated structures and conditions, where purely analytical solutions become cumbersome. The thermal quadrupole method can be effectively used to model heat conduction problems in multilayer systems. Needless to say, multiple NDT methods can be applied to reach a more comprehensive understanding of an ancient artifact.

Acknowledgements
Not applicable.

Author contributions
XY and CBC conceptualized the experiment and prepared the original draft. GH, XW, WF and JZ designed and conducted the experiment. NT and GY supervised the work and reviewed the manuscript. All authors read and approved the final manuscript.

Funding
This work is funded by the National Social Science Fund of China (No. 19CKG024) and Beijing Municipal Office of Philosophy and Social Science Planning (SM202010028006).

Availability of data and materials
The datasets used and/or analyzed during the current study are available from the corresponding author on reasonable request.

Declarations

Competing interests
The authors declare that they have no competing interests.

Author details
[1]Key Laboratory of Terahertz Optoelectronics, Ministry of Education, and Beijing Advanced Innovation Center for Imaging Theory and Technology, Department of Physics, Capital Normal University, 105 West Third Ring Road North, Beijing 100048, China. [2]School of History, Capital Normal University, 83 West Third Ring Road North, Beijing 100089, China.

Received: 13 July 2022 Accepted: 21 September 2022
Published online: 29 September 2022

References

1. Michio M. The manufacturing background of Western Zhou bronzes. In: Bulletin of the Tokyo University Institute of Oriental Culture. Tokyo: Institute of Oriental Culture, University of Tokyo; 1977.
2. Rawson J. Western Zhou ritual bronzes from the Arthur M. Sackler collections. Washington, D.C.: Arthur M. Sackler Foundation, 1990. ISBN 9780674950702
3. Su R, Hu D. The use and abuse of Shang and Zhou bronzes **商周铸吉金中垫片的使用和滥用**. In: Bulletin of the Jao Tsung-I Academy of Sinology **饶宗颐国学院院刊**. Hong Kong: Chung Hwa Books; 2014. p. 101–34. ISSN 2310–9297 (**In Chinese**).
4. Hu D. X-ray Imaging of artifacts**文物的**X**射线成像**. Beijing: Science Publishing House; 2012. (**(In Chinese)**).
5. Maldague X. Theory and practice of infrared technology for nondestructive testing. New York: Wiley; 2001.
6. Maldague X, Marinetti S. Pulse phase infrared thermography. J Appl Phys. 1996;79(5):2694–8. https://doi.org/10.1063/1.362662.
7. Scudieri F, Mercuri F, Volterri R. Non-invasive analysis of artistic heritage and archaeological findings by time resolved IR thermography. J Thermal Anal Calorim. 2001;66:307–14. https://doi.org/10.1023/A:1012420622561.
8. Mercuri F, Zammit U, Orazi N, Paoloni S, Marinelli M, Scudieri F. Active infrared thermography applied to the investigation of art and historic artefacts. J Thermal Anal Calorim. 2011;104:475–85. https://doi.org/10.1007/s10973-011-1450-8.
9. Orazi N. The study of artistic bronzes by infrared thermography: A review. J Cult Herit. 2020;42:280–9. https://doi.org/10.1016/j.culher.2019.08.005.
10. Grinzato E, Bressan C, Marinetti S, Bison P, Bonacina C. Monitoring of the Scrovegni Chapel by IR thermography: Giotto at infrared. Infrared Phys Technol. 2002;43:165–9. https://doi.org/10.1016/S1350-4495(02)00136-6.
11. Brooke C. Thermal imaging for the archaeological investigation of historic buildings. Remote Sens. 2018;10(9):1401. https://doi.org/10.3390/rs10091401.
12. Zhang H, Sfarra S, Saluja K, Peeters J, Fleuret J, Duan Y, Fernandes H, Avdelidis N, Ibarra-Castanedo C, Maldague X. Non-destructive investigation of paintings on canvas by continuous wave terahertz imaging and flash thermography. J Nondestruct Eval. 2017;36(2):34. https://doi.org/10.1007/s10921-017-0414-8.
13. Bodnar JL, Candoré JC, Nicolas JL, Szatanik G, Detalle V, Vallet JM. Stimulated infrared thermography applied to help restoring mural paintings. NDT&E Int. 2012;49:40–6. https://doi.org/10.1016/j.ndteint.2012.03.007.
14. Grinzato E, Bison P, Marinetti S, Vavilov V. Nondestructive evaluation of delaminations in fresco plaster using transient infrared thermography. J Nondestruct Eval. 1996;5(4):257–74. https://doi.org/10.1007/BF01606462.
15. Avdelidis N, Koui M, Ibarra-Castanedo C, Maldague X. Thermographic studies of plastered mosaics. Infrared Phys Technol. 2007;49:254–6. https://doi.org/10.1016/j.infrared.2006.06.027.
16. Theodorakeas P, Avdelidis NP, Cheilakou E, Koui M. Quantitative analysis of plastered mosaics by means of active infrared thermography. Constr Build Mater. 2014;73:417–25. https://doi.org/10.1016/j.conbuildmat.2014.09.089.
17. Bottoni M, Fabretti G. Model for the analysis of sun radiation structures exposed to open air: consideration of its validity and usefulness based on its experimentation in situ. In: Proceedings Volume 4360, Thermosense XXIII. Orlando, FL, United States; 2001. https://doi.org/10.1117/12.421051.
18. Orazi N, Mercuri F, Zammit U, Paoloni S, Marinelli M, Giuffredi A, Salerno CS. Thermographic analysis of bronze sculptures. Stud Conserv. 2016;61(4):236–44. https://doi.org/10.1179/2047058415Y.0000000025.
19. Mercuri F, Caruso G, Orazi N, Zammit U, Cicero C, Colacicchi Alessandri O, Ferretti M, Paoloni S. Interface thermal conductance characterization by infrared thermography: a tool for the study of insertions in bronze ancient Statuary. Infrared Phys Technol. 2018;90:31–9. https://doi.org/10.1016/j.infrared.2018.02.002.
20. Orazi N, Paoloni S, Zammit U, Cicero C, Ferretti M, Caruso G, Colacicchi Alessandri O, Paris R, Mercuri F. Thermographic investigation of bronzeartefacts: characterization of structure elements and casting faults in masterpieces of the bronze statuary of Rome. Int J Thermophys. 2018;39(12):141. https://doi.org/10.1007/s10765-018-2467-z.
21. Mercuri F, Paoloni S, Orazi N, Cicero C, Zammit U. Pulsed infrared thermograph applied to quantitative characterization of the structure and the casting faults of the Capitoline She Wolf. Appl Phys A. 2017;123(5):327. https://doi.org/10.1007/s00339-017-0958-6.
22. Tao N, Wang C, Zhang C, Sun JG. Quantitative measurement of cast metal relics by pulsed thermal imaging. QIRT J. 2020;19(1):27–40. https://doi.org/10.1080/17686733.2020.1799304.
23. Mercuri F, Caruso G, Orazi N, Zammit U, Ceccarelli S, Cicero C, Vadrucci M, Paoloni S. Depth-resolved analysis of double-layered cultural heritage artifacts by pulsed thermography. Int J Thermophys. 2020;41:6. https://doi.org/10.1007/s10765-019-2587-0.
24. Maldague X. Nondestructive evaluation of materials by infrared thermography. New York: Springer; 1993. https://doi.org/10.1016/S0963-8695(97)87789-4.
25. Parker WJ, Jenkins RJ, Butler CP, Abbott GL. Flash method of determining thermal diffusivity, heat capacity, and thermal conductivity. J Appl Phys. 1961;32(9):1679–84. https://doi.org/10.1063/1.1728417.
26. Balageas D, Krapez J, Cielo P. Pulsed photothermal modeling of layered materials. J Appl Phys. 1986;59(2):348–57. https://doi.org/10.1063/1.336690.
27. Shepard SM, Lhota JR, Rubadeux BA, Wang D, Ahmed T. Reconstruction and enhancement of active thermographic image sequences. Opt Eng. 2003;42(5):1337–42. https://doi.org/10.1117/1.1566969.
28. Lau SK, Almond DP, Patel PM. Transient thermal wave techniques for the evaluation of surface coatings. J Phys D: Appl Phys. 1991;24(3):428–36. https://doi.org/10.1088/0022-3727/24/3/029.
29. Tao N, Li XL, Sun JG. Simultaneous measurement of thermal conductivity and heat capacity by flash thermal imaging methods. Rev Sci Instrum. 2017;88(6): 064903. https://doi.org/10.1063/1.4985633.
30. Maillet D, André S, Batsale JC, Degiovanni A, Moyne C. Thermal Quadrupoles. Chichester: Wiley; 2000.
31. Bendada A, Erchiqui F, Lamontagne M. Pulsed thermography in the evaluation of an aircraft composite using 3D thermal quadrupoles and mathematical perturbations. Inverse Probl. 2005;21:857–77. https://doi.org/10.1088/0266-5611/21/3/005.
32. Sun JG. Analysis of pulsed thermography methods for defect depth prediction. J Heat Transfer. 2006;128(4):329–38. https://doi.org/10.1115/1.2165211.
33. Lamrani M, Laaroussi N, Khabbazi A, Khalfaoui M, Garoum M, Feiz A. Experimental study of thermal properties of a new ecological building material based on peanut shells and plaster. Case Stud Constr Mat. 2017;7(3):294–304. https://doi.org/10.1016/j.cscm.2017.09.006.

Publisher's Note